nature energy

Article

https://doi.org/10.1038/s41560-026-02032-7

Thermal runaway-free ampere-hour-level Na-ion battery via polymerizable non-flammable electrolyte

Received: 22 May 2025

Accepted: 9 March 2026

Published online: 06 April 2026

Check for updates

Jiao Zhang[1,2], Lin Zhou[1], Haibo Wang[1,3], Suting Weng[1], Shuai Han[1], Yang Yang[1,3], Yuan Liu[1,3], Zhao Chen[1,3], Xubin Wang[1,3], Feixiang Ding[1,2], Fei Xie[1] ✉, Huican Mao[4] ✉, Xuefeng Wang[1], Yaxiang Lu[1,2] ✉, Liquan Chen[1] & Yong-Sheng Hu[1,2,3,5,6] ✉

Safety is the most basic requirement for the application of rechargeable batteries in large-scale energy storage. Despite extensive efforts in developing non-flammable electrolytes, the elimination of thermal runaway in ampere-hour-level cells remains unachieved, while the correlation between electrolyte flame retardancy and battery safety is still unclear. Here we propose a polymerizable and non-flammable electrolyte, which leverages the synergistic anion–cation solvation effect and undergoes thermally triggered polymerization. The optimized electrode–electrolyte interfacial and a cross-linked barrier were obtained to prevent mechanical/chemical interactions between the electrodes and impede the side reactions/reductive gases generation, leading to no thermal runaway in ampere-hour-level cells. The nail-penetration tests were also passed without smoke, fire or explosion. This work brings an insight of the battery safety beyond non-flammable electrolyte design and paves the way towards safer and more efficient battery systems for energy storage.

Battery safety is always a paramount issue in energy storage applications[1–6]. A series of exothermic reactions can gradually occur under the conditions of battery abuse, such as collision, overcharge/discharge, high-temperature operation and so on, accumulating a large amount of heat and causing thermal runaway with even fire and explosion[3,7]. Traditional carbonate ester-based organic electrolytes are prone to fire or explosion hazards due to their flammability when short circuit or thermal runaway occurs[3,8]. To solve this problem, phosphate esters have been proven to be a proper candidate for the design of non-flammable electrolytes[3,9–11] because of the nature that their decomposition products at high temperatures can react with hydrogen free radicals in the combustion products[12].

Nevertheless, most of the early studies about such non-flammable electrolytes only pay attention to whether the electrolyte design can successfully impede the flammability. In recent years, although a few investigations on the non-flammable electrolytes for Li-ion batteries (LIBs) have incorporated reports on battery-level safety, there is almost no such report for Na-ion batteries (NIBs) (Fig. 1a). It was also reported that the battery using trimethyl phosphate (TMP)-based non-flammable electrolyte still underwent the occurrence of thermal runaway[2,13], suggesting that a non-flammable electrolyte has not yet been able to guarantee the intrinsic safety of ampere-hour-level cells[3,9,14–19] (Fig. 1b). Therefore, the thermal stability of the electrolyte itself, the stability of the electrode–electrolyte interfaces and the

[1]Key Laboratory for Renewable Energy, Beijing Key Laboratory for New Energy Materials and Devices, Beijing National Laboratory for Condensed Matter Physics, Institute of Physics, Chinese Academy of Sciences, Beijing, China. [2]Huairou Division, Institute of Physics, Chinese Academy of Sciences, Beijing, China. [3]College of Materials Science and Optoelectronic Technology, University of Chinese Academy of Sciences, Beijing, China. [4]Department of Materials Science, Key Laboratory of Automobile Materials, MOE and International Center of Future Science, Jilin University, Changchun, China. [5]HiNa Battery Technology Co. Ltd., Beijing, China. [6]Yangtze River Delta Physics Research Center Co. Ltd, Liyang, China. ✉e-mail: fxie@iphy.ac.cn; hcmao@jlu.edu.cn; yxlu@iphy.ac.cn; yshu@iphy.ac.cn

https://doi.org/10.1038/s41560-026-02032-7

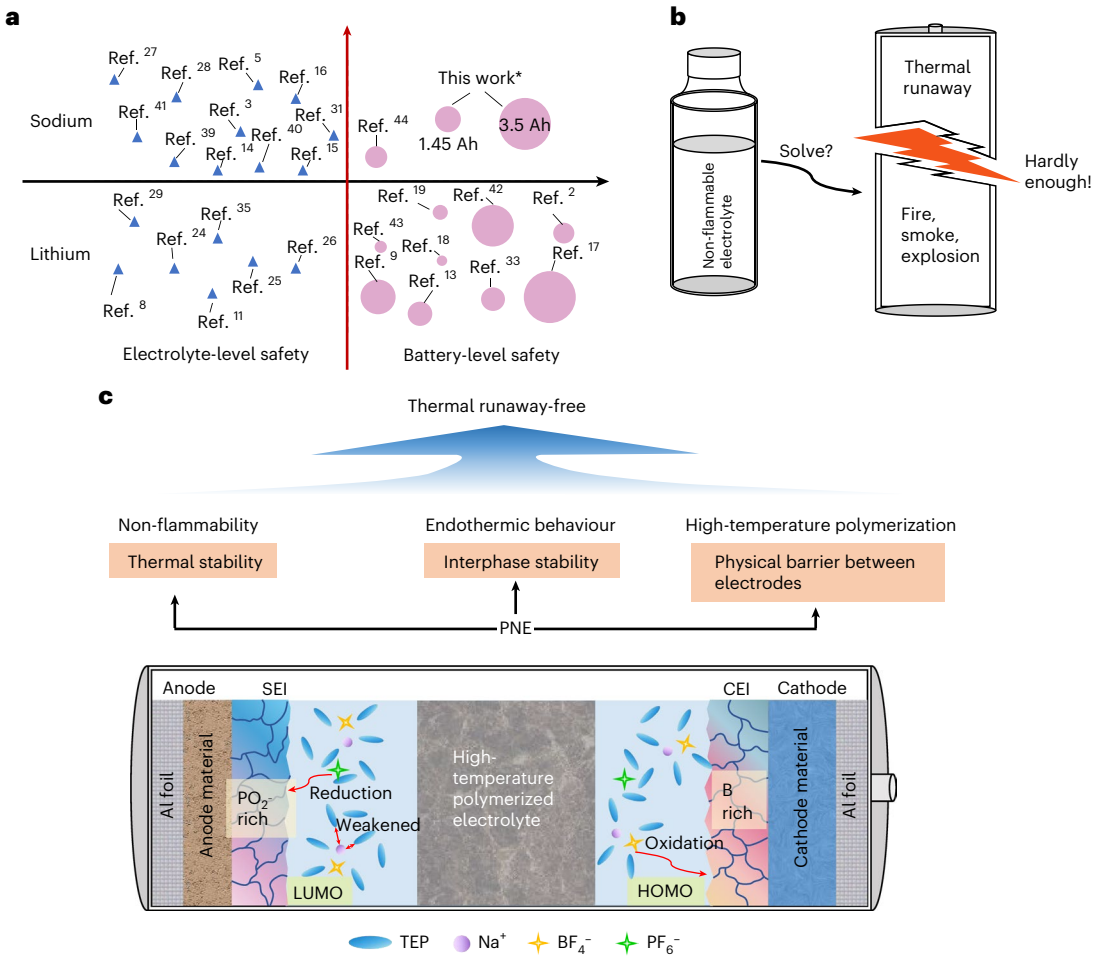

Fig. 1 | The importance of batteries safety and the comparison of our work with previous corresponding works. a, A summary of literature studies on presentation or discussion about electrolyte-level safety or battery-level safety of sodium and lithium-ion batteries. The size of the circle represents the capacity of the battery shown in the literature; the larger the circle, the larger the battery capacity. The smallest circle represents coin cells. This work*: 1.45 Ah and 3.5 Ah cylindrical battery passed the nail-penetration test with no fire, no smoke and no explosion, and passed the 300 °C ARC and thermal abuse tests. Electrolyte-level safety: only the non-flammability was discussed. Refs. 8,11,23–25,28,34: LIBs; refs. 5,14–16,26,27,30,64–66: NIBs. Battery-level safety: refs. 2,9,13,17–19,32,67,68: LIBs; ref. 69: NIBs. Detailed analysis is presented in Supplementary Table 1. **b**, A common misconception in most current research is that if the electrolyte is flame retardant, the safety of the battery can be improved. However, this study finds that even flame-retardant electrolytes can still cause severe thermal runaway. In other words, flame retardancy does not equal safety. **c**, Schematic illustration of PNE exhibiting thermal runaway-free performance.

interactions between the anode and cathode at high temperatures need to be considered comprehensively.

In addition, although phosphate esters exhibit many advantages such as a broad liquid range (contributing to wide-temperature compatibility), high salt solubility and notable cost effectiveness, their practical performance as non-flammable electrolyte solvents in rechargeable batteries has also been limited by the poor compatibility with carbon-based anodes[3,5,9,11,21–24]. Strategies such as high-concentration[3,5,9,11,21–24] (including localized high-concentration[25–27]) or fluorinated systems[8,13,17,25,28–32] and so on[16,18,33,34] can improve the compatibility but increase cost and complexity. Consequently, it is also of great significance to develop a manufactured non-flammable electrolyte with optimized solvation structure and interfacial chemistry without resorting to high salt concentration or fluorination towards both the excellent electrode compatibility and battery safety.

Here we propose a polymerizable and non-flammable electrolyte (PolyNonflyte or PNE). This design not only achieves the non-flammability but also enables the thermal self-protection through in situ polymerization of phosphoric acid, a decomposition product of triethyl phosphate (TEP)[35–37], forming an insulating polymer network to block the mechanical and chemical crosstalk between cathode and anode at high temperature. Besides, the co-existence of BF_4^- and PF_6^- anions attenuates the Na^+-solvent binding and contributes to the optimized formation of a B^--rich cathode electrolyte interphase (CEI) and PO_2^--rich solid electrolyte interphase (SEI), which further enhances the electrochemical and thermal stability (Fig. 1c). As a result, no thermal runaway was detected in 3.5-Ah cylindrical cells, even at a high temperature of 300 °C. The nail-penetration test was also successfully passed without fire or explosion. In addition, the PNE electrolyte is further implemented in a 4.3-V high-voltage pouch cylindrical cell, realizing a high energy density of 211 Wh kg^{-1} and successful satisfaction with the nail-penetration safety test. This work offers a perspective on electrolyte design beyond non-flammability in high-performance and safe NIBs, thereby laying the foundation for the development of energy storage applications.

The characteristics of PNE

The polyethylene separators were immersed in different solvent-based electrolytes and subjected to a subsequent ignition experiment (Fig. 2a) to verify the non-flammability of each electrolyte. The components of all the electrolyte samples have been displayed in Supplementary Table 2. Only the separators soaked in the TEP-based and TMP-based electrolytes

https://doi.org/10.1038/s41560-026-02032-7

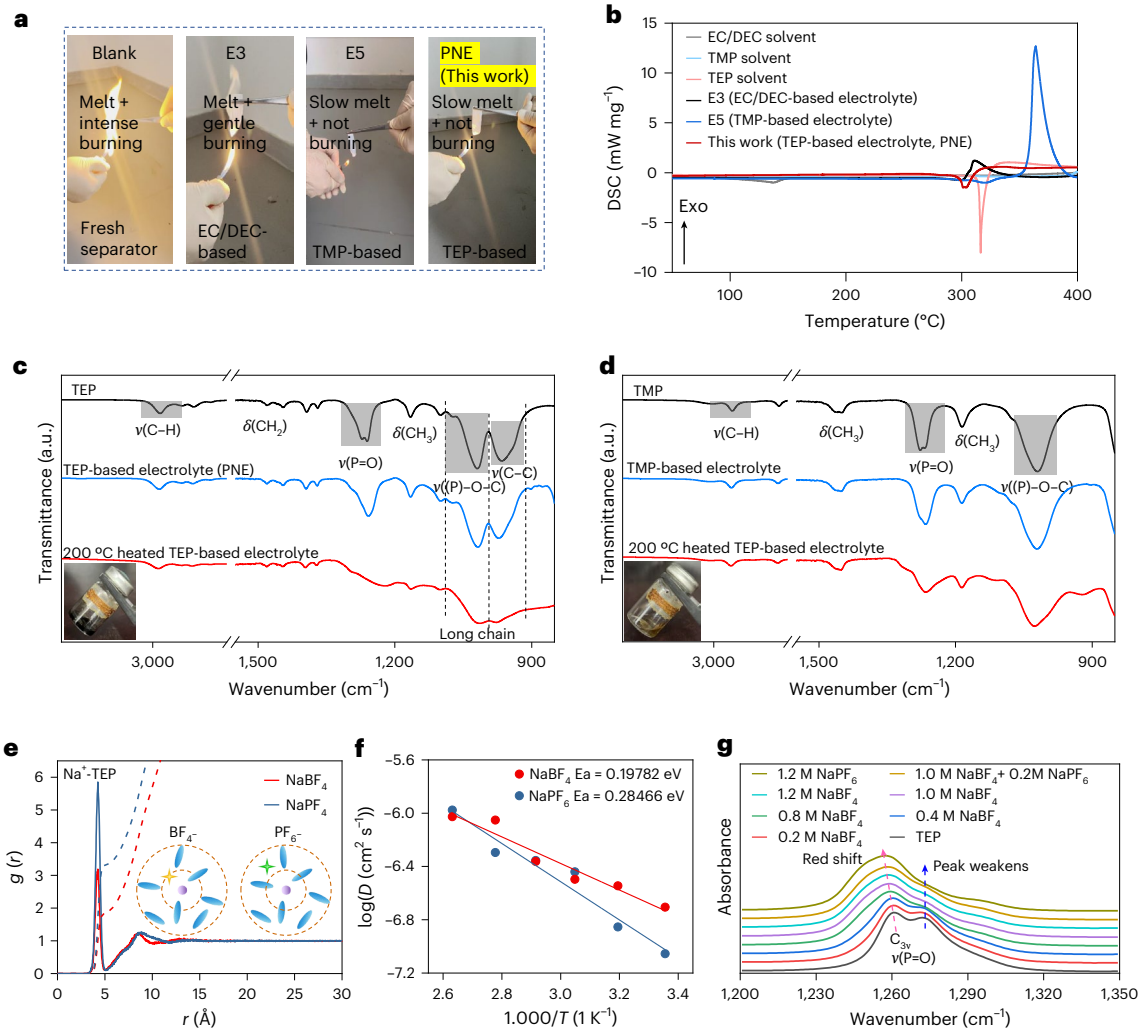

Fig. 2 | The characteristics of PNE. a, Ignition experiment of fresh separator and the separators immersed in EC/DEC-based electrolyte (E3), TMP-based electrolyte (E5) and TEP-based electrolyte (PNE). **b**, DSC measurement of the above electrolytes and the corresponding solvents. **c**, FTIR spectra of TEP solvent, PNE and 200 °C heated PNE. The embedded picture is heated PNE under 200 °C. **d**, FTIR spectra of TMP solvent, E5 and 200 °C heated E5. The embedded picture is heated E5 under 200 °C. **e**, The radial distribution function and corresponding donor number (DN) values of Na^+ to TEP within $NaPF_6$ or $NaBF_4$. The embedded diagram depicts the structural arrangement of the first solvation shell. **f**, Activation energies of Na^+ desolvation (Ea) with $NaPF_6$ or $NaBF_4$ in TEP-based electrolyte. **g**, The infrared absorption spectra of electrolytes based on TEP with varying concentrations.

did not combust (Supplementary Videos 1–4 provide detailed information), indicating their excellent non-flammability. We further conducted thermal stability tests on the three groups of electrolytes and the corresponding solvents using differential scanning calorimeter (DSC) (Fig. 2b). The results show that the TEP-based PNE exhibited notable endothermic behaviour as the temperature increased, which is probably due to the inherent endothermic nature of TEP itself. In contrast, both the ethylene carbonate (EC)/diethyl carbonate (DEC)-based and the non-flammable TMP-based electrolytes showed distinct exothermic behaviour. Notably, the exothermic behaviour of the TMP-based electrolyte was even more pronounced than that of the EC/DEC-based electrolyte. These findings reveal that the three electrolytes present completely different decomposition behaviours at high temperatures. The endothermic decomposition reaction of TEP is highly advantageous for battery safety. To further investigate the thermal stability of the three electrolytes, they were subjected to heating at 200 °C, a temperature commonly associated with the onset of thermal runaway in most battery systems. As depicted in Supplementary Fig. 1, the EC/DEC-based electrolyte underwent nearly complete decomposition upon heating. In contrast, the TMP-based electrolyte retained its liquid state but exhibited a colour change from colourless and transparent to yellow and transparent, which is indicative of partial decomposition. Surprisingly, the TEP-based PNE turned from a colourless and transparent liquid to a brownish and viscous substance, indicating a thermally induced polymerization at high temperature.

The polymerization reaction was further investigated using infrared spectroscopy (Fig. 2c). The C–H vibration peaks in the PNE were weakened after being heated at 200 °C, while the vibration characteristic peaks of the P=O, P–O–C and C–C bonds were significantly broadened, which proves the polymerization of PNE with long chains at high temperature[38]. It was reported before that TEP would decompose by losing ethyl groups to form phosphoric acid[35,36]. Therefore, the polymerization detected here is probably due to the further polymerization of phosphoric acid generated from the decomposition of TEP. In contrast, the peaks for the TMP-based electrolyte show almost no change, which suggests that the TMP-based electrolyte did not undergo such polymerization process (Fig. 2d). It is evident that although TMP and TEP both possess non-flammable characteristics, their thermal stability and thermal reaction behaviours are remarkably different, which also implies their roles in battery safety.

High-resolution mass spectrometry was used to further elucidate the polymerization pathway of PNE. As shown in Supplementary Fig. 2,

before heating, the detected species were almost exclusively below $m/z = 400$ and were dominated by $Na^+(TEP)_1$ and $Na^+(TEP)_2$ clusters. After heating to 200 °C, the distribution markedly shifted to m/z values above 500. On the basis of accurate-mass analysis, the predominant peak at m/z 685 most likely corresponds to a $(TEP)_6$ oligomer. The proposed molecular structure is shown in Supplementary Fig. 3.

Despite TEP's excellent thermal stability owing to its flame-retardant effect and thermally induced polymerization, the compatibility with electrodes, especially for hard carbon (HC) anodes, must be addressed for its practical application in batteries. This can be tackled from two main aspects: (1) weakening the solvation interaction between TEP and Na^+ to facilitate the desolvation process on the HC surface; (2) optimizing interfacial chemistry to construct stable CEI and SEI. On the basis of this principle, the salts with proper anions are supposed to be controlled. Sodium hexafluorophosphate ($NaPF_6$) is one of the most widely used sodium salts with low cost and high ionic conductivity. However, it is speculated that PF_6^- has a large size and is difficult to enter the first solvation layer of Na^+, so the binding force between Na^+ and phosphate esters is strong in $NaPF_6$-based electrolytes, which has a negative impact on the anode compatibility. Therefore, the smaller-sized and cheaper sodium tetrafluoroborate ($NaBF_4$) was selected. The molecular dynamics (MD) simulation results show that the coordination number values of TEP in the $NaPF_6$ and $NaBF_4$-based electrolytes are 3.3 and 1.8 (Fig. 2e), respectively, which means that the number of TEP solvent molecules presenting in the first solvation shell of Na^+ is reduced in the $NaBF_4$-based electrolyte. This phenomenon can be attributed to the smaller molecular volume of BF_4^- compared to PF_6^-, which enhances its ability to displace surrounding solvent molecules around Na^+. Activation energies towards Na^+ desolvation in $NaBF_4$ and $NaPF_6$-based electrolytes are determined to be 0.19782 eV and 0.28466 eV, respectively, thereby reinforcing the notion that the inclusion of BF_4^- effectively promotes the desolvation mechanism for Na^+ (Fig. 2f).

The infrared test results of the series of electrolytes further verified that the presence of BF_4^- can weaken the interaction between Na^+ and solvent molecules. The infrared peaks observed at 1,260 cm^{-1} and 1,272 cm^{-1} correspond to the P=O bonds of TEP in C_{3v} and C_3 conformers, respectively[39]. Intramolecular hydrogen bonding between the alkyl hydrogens and the phosphoryl oxygen probably leads to a lowering of the P=O frequency in the case of the C_{3v} conformer[40], whereas C_3 conformer does not involve any intramolecular interactions[40]. It is noteworthy that the solvation between Na^+ with TEP predominantly occurs at the P=O bond, and the binding with the metal ion weakens the P=O bond, causing a redshift in its vibrational frequency[41]. Therefore, the extent of the infrared vibrational frequency shift of the P=O bond can be used as an indicator to assess the strength of solvation. As shown in Fig. 2g, with the increase in Na^+ concentration, the redshift distance of the P=O bond gradually increases. This indicates that the higher the salt concentration, the stronger the solvation effect. Moreover, when comparing the electrolytes with the same concentration of $NaBF_4$ and $NaPF_6$, the red-shift distance of the P=O bond is greater in $NaPF_6$, which implies that the solvation effect of TEP is weaker in $NaBF_4$. Therefore, the use of $NaBF_4$ can weaken the solvation effect between Na^+ and TEP, thereby achieving compatibility between TEP and the HC anode. The reason why we did not use $NaBF_4$ exclusively is due to concerns about interface formation, which will be analysed in detail later.

The coordination between the salts and non-flammable solvents towards the electrode compatibility was further investigated using electrospray ionization mass spectrometry (ESI-MS) to characterize the solvation structure of 1.0 M $NaPF_6$ in TEP/TMP (1/1) electrolyte (Supplementary Fig. 4). ESI-MS has been verified to be an effective and reliable tool for quantitative analysis of solvation sheath structure[42–44], and the solvation sheath structure as revealed by ESI-MS should be closer to the edge sites of anode during the charging process[42]. The result shows that $Na^+(TEP)_2$ remains the most abundant species, followed by $Na^+(TEP)_1$, $Na^+(TEP)_1(TMP)_1$ and $Na^+(TMP)_3$ and so on, meaning that Na^+ is preferentially solvated with TEP on the edge sites of anode. MD simulations also verified this point. In the TMP-based electrolytes, the Na^+ desolvation energies are lower than those in TEP-based electrolytes with both $NaPF_6$ and $NaBF_4$ (Fig. 2f and Supplementary Fig. 5). These results imply that the TMP-based electrolytes are supposed to hold the greater potential for superior performance in batteries. However, it is unexpected that a higher first-cycle Coulombic efficiency (Supplementary Fig. 6) and better cycling stability (Supplementary Fig. 7) with TEP-based electrolyte are delivered than the TMP-based electrolyte based on the 2032 coin-type full cells. This contrast suggests that the solvation structure is not the only key factor in determining battery performance, while the stability of the electrode–electrolyte interfaces must also be considered.

Electrode–electrolyte interfaces based on PNE

As shown by the cryo-transmission electron microscopy (cryo-TEM), the SEI film formed in the PNE electrolyte after ten cycles appears to be a uniform and thin layer (4.8 nm) covering the surface of the anode (Fig. 3a). Conversely, the SEI films formed in EC/DEC-based electrolyte and TMP-based electrolyte are non-uniform with greater thicknesses of 12.5 nm and 6.89 nm, respectively. Furthermore, time of flight secondary ion mass spectrometry (TOF-SIMS) reveals that the SEI generated in the three electrolytes contained F^- and PO_2^- groups (Fig. 3b and Supplementary Fig. 8). Due to the lower lowest unoccupied molecular orbital (LUMO) energy level compared to $NaBF_4$ (Fig. 3c), it can be inferred that $NaPF_6$ preferentially decomposes on the HC surface, resulting in an SEI rich in F^- and PO_2^- groups. The much larger amounts of the two groups on the interface of HC cycled in EC/DEC-based E3 electrolyte compared to E5 and PNE can be attributed to the higher concentration of $NaPF_6$. This also suggests that the F^-- and PO_2^--rich SEI is good for the HC because E3 is a well-studied electrolyte for NIBs with excellent compatibility with carbon anodes. Although PNE and E5 exhibit fewer F^- and PO_2^- groups and are mainly located at the surface of the SEI compared to E3 due to the lower concentration of $NaPF_6$, the higher amount of these species of PNE, in particular the PO_2^-, contribute to the better compatibility with carbon anodes compared to E5 (Fig. 3b and Supplementary Figs. 8 and 9). Moreover, the content of PO_2^- in the EC/DEC system increases with the etching depth (for details, Supplementary Fig. 9 provides the etching depth profile), which may be associated with the dissolution of transition metal ions[45]. In contrast, in the TMP and TEP systems, the PO_2^- signal exhibited rapid attenuation from the outer surface to the inner layers, indicating that the further decomposition of $NaPF_6$ was effectively suppressed. On the basis of these observations, we can conclude that a higher content of PO_2^- at the interface would be more conducive to the compatibility with the HC anode.

Meanwhile, the formation of CEI film on the cathode with PNE electrolyte is more uniform and thinner (9.83 nm) than those of E3 and E5 electrolytes. Due to the higher highest occupied molecular orbital (HOMO) of $NaBF_4$ compared to $NaPF_6$, B-rich CEI can easily form on the cathode surface (Fig. 3a–c and Supplementary Fig. 9). We also analysed the content of transition metal elements on the anode after cycling in the PNE electrolyte via inductively coupled plasma spectroscopy (ICP) and found that the residual contents of the transition metals, such as Ni, Fe, Mn and Cu, are lower than those in E3 and E5. These transition metals can only come from the cathode side, suggesting that the optimized B-rich CEI can inhibit the dissolution of transition metals from the cathodes (Fig. 3d), which lays the foundation for achieving high voltage and cycling stability. It is also found that the greater high-voltage stability of phosphate esters (TEP and TMP) than that of EC/DEC electrolytes was indicated by the linear sweep voltammetry (LSV) measurement, where the voltage window of TEP is even wider than that of TMP (Supplementary Fig. 10).

https://doi.org/10.1038/s41560-026-02032-7

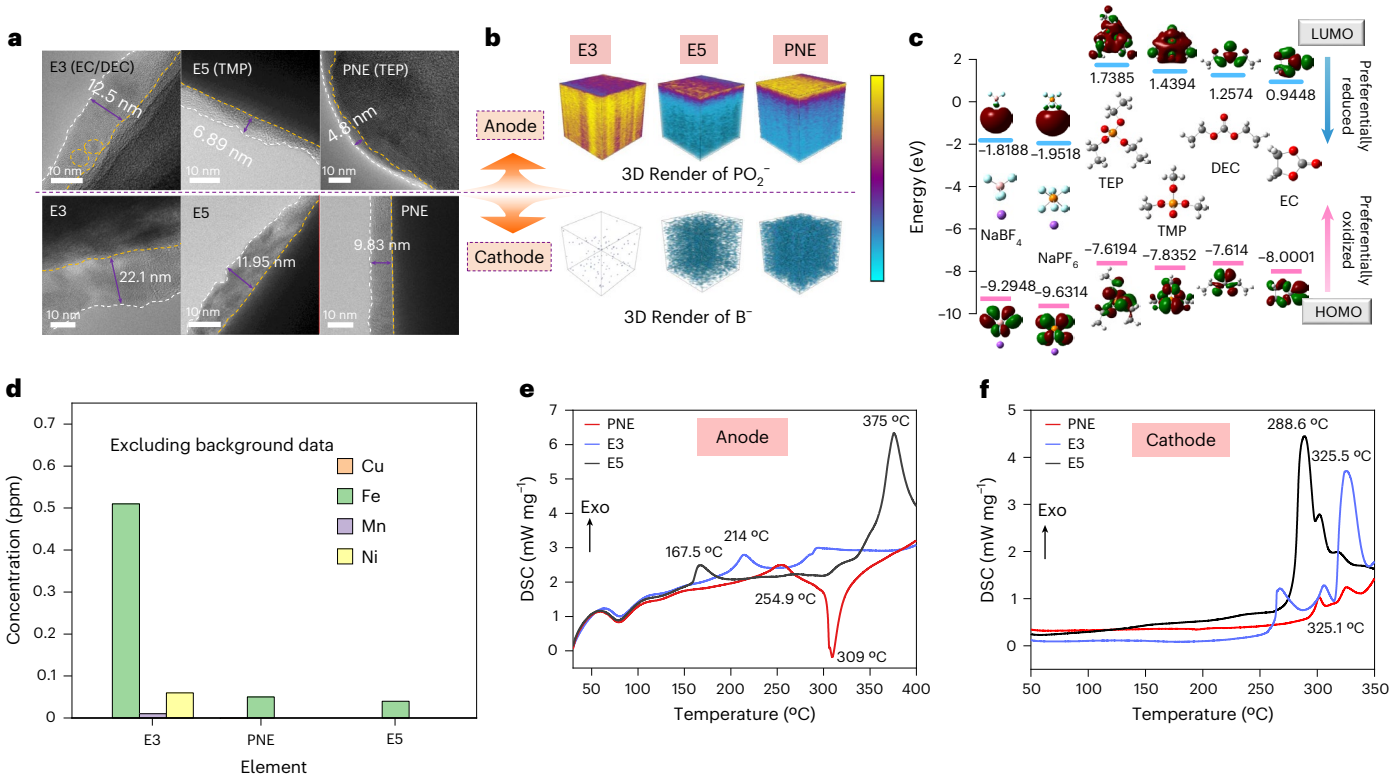

Fig. 3 | The interface characterization of cathode and anode materials. **a**, Annular bright field cryo-STEM image of HC and O3-$NaCu_{1/9}Ni_{2/9}Fe_{1/3}Mn_{1/3}O_2$ (CNFM) in E3 (EC/DEC-based) or PNE (the designed) after ten cycles. **b**, TOF-SIMS three-dimensional views of the SEI films and CEI films. **c**, Molecular orbital energies of $NaBF_4$, $NaPF_6$, TEP, TMP, DEC and EC including LUMO energies and HOMO energies. Colours for different atoms: white for H, purple for Na, grey for C, red for O, orange for P, blue for F and pink for B. The positive and negative phases of HOMO–LUMO orbitals are represented in red and green regions. **d**, The amount of transition metals (Ni, Fe, Mn and Cu) deposited on the cycled HC anode (ten cycles) from ICP results. **e**,**f**, Thermal stability for anode materials and cathode materials disassembled from an HC//CNFM 2032 coin cells charged to 3.95 V in the DSC testing.

Thermal stability of the electrodes with PNE

DSC tests were performed to investigate the thermal stability of desodiated cathodes and sodiated anodes upon disassembly of the charged coin-type full cells in different electrolytes.

The heat release of the HC anode in the electrolyte can be roughly divided into three stages[46]: (1) a heat release resulting from the decomposition of SEI; (2) a heat release occurring between the electrolyte and the inserted Na^+ in the carbon anode, accompanied by repeated formation of new SEI;[3] (3) as the reaction progresses and exposes the internal surface of the electrode, further heat is released due to the reaction between the anode, electrolyte and binder[47]. As shown in Fig. 3e, for the PNE system, the heat release from SEI decomposition in the initial stage of the designed system is negligible, whereas the heat release during the second stage reaction is also minimal compared to E3 and E5 systems. Most importantly, an endothermic peak at 309 °C is still observed, which is consistent with the thermal behaviour of the electrolyte (Fig. 2b). This indicates a weak side reaction between PNE and the carbon anode, such that the endothermic behaviour intrinsic to the electrolyte itself dominates the overall thermal response. Additionally, the evaporation and heat dissipation of the electrolyte in such high temperature may further amplify such endothermic response in the DSC curve.

The exothermic reactions of the cathode material in electrolyte could be arisen from three processes[48]: (1) structural transformation of the active material due to transition metal migration[2]; (2) decomposition of the organic electrolytes[49]; and (3) redox reaction between electrophilic alkyl carbonate solvent in the electrolyte and nucleophilic superoxide or peroxide species generated by electrolytic oxidation[50]. The prominent peaks after 250 °C can be attributed to vigorous interactions between the generated O_2 and the electrolyte, resulting in significant heat generation that is adequate to initiate a thermal runaway in the battery. However, the cathode with designed PNE electrolyte demonstrates a limited and exothermic peak of DSC, indicating effective inhibition of further reaction between the electrolyte and the material at the cathode–electrolyte interface (Fig. 3f). It is also suggested that the intrinsic endothermic behaviour and thermal polymerization of the PNE electrolyte can offset the majority of the heat generated from the limited reactions (Fig. 3f).

In addition, we have performed simultaneous thermogravimetry–differential scanning calorimetry–mass spectrometry (TG–DSC–MS) measurements for sodiated anode and desodiated cathode sheets individually mixed with the three electrolytes (E3 (EC-DEC-based), E5 (TMP-based) and PNE (TEP-based)). The charge-to-mass ratios and the corresponding gaseous species are listed in Supplementary Table 3. Compared with E3 and E5, PNE generates fewer reductive gases, indicating suppressed parasitic reactions. Detailed comparisons are shown following Supplementary Figs. 11 and 12.

Safety of the PNE-based ampere-hour-level NIBs

To validate the feasibility of using the non-fluorinated and non-flammable TEP-based PNE electrolyte in practical applications, commercial 18650 (1.45 Ah) and 26700 (3.5 Ah) cylindrical cells with HC anodes and O3-$NaCu_{1/9}Ni_{2/9}Fe_{1/3}Mn_{1/3}O_2$ (CNFM) cathodes were tested. In the nail-penetration tests of the 18650 cylindrical cells (Fig. 4a), the conventional carbonate system (E3) and the TMP system (E5) experienced smoke, fire and explosion (Supplementary Videos 5 and 6). Conversely, TEP-based electrolyte (PNE) has been verified to have no smoke, fire or explosion upon the nail-penetration test in both 18650 and 26700 cells (Supplementary Videos 7 and 8), suggesting the high safety of the PNE-based NIBs. Additionally, it was observed that during

https://doi.org/10.1038/s41560-026-02032-7

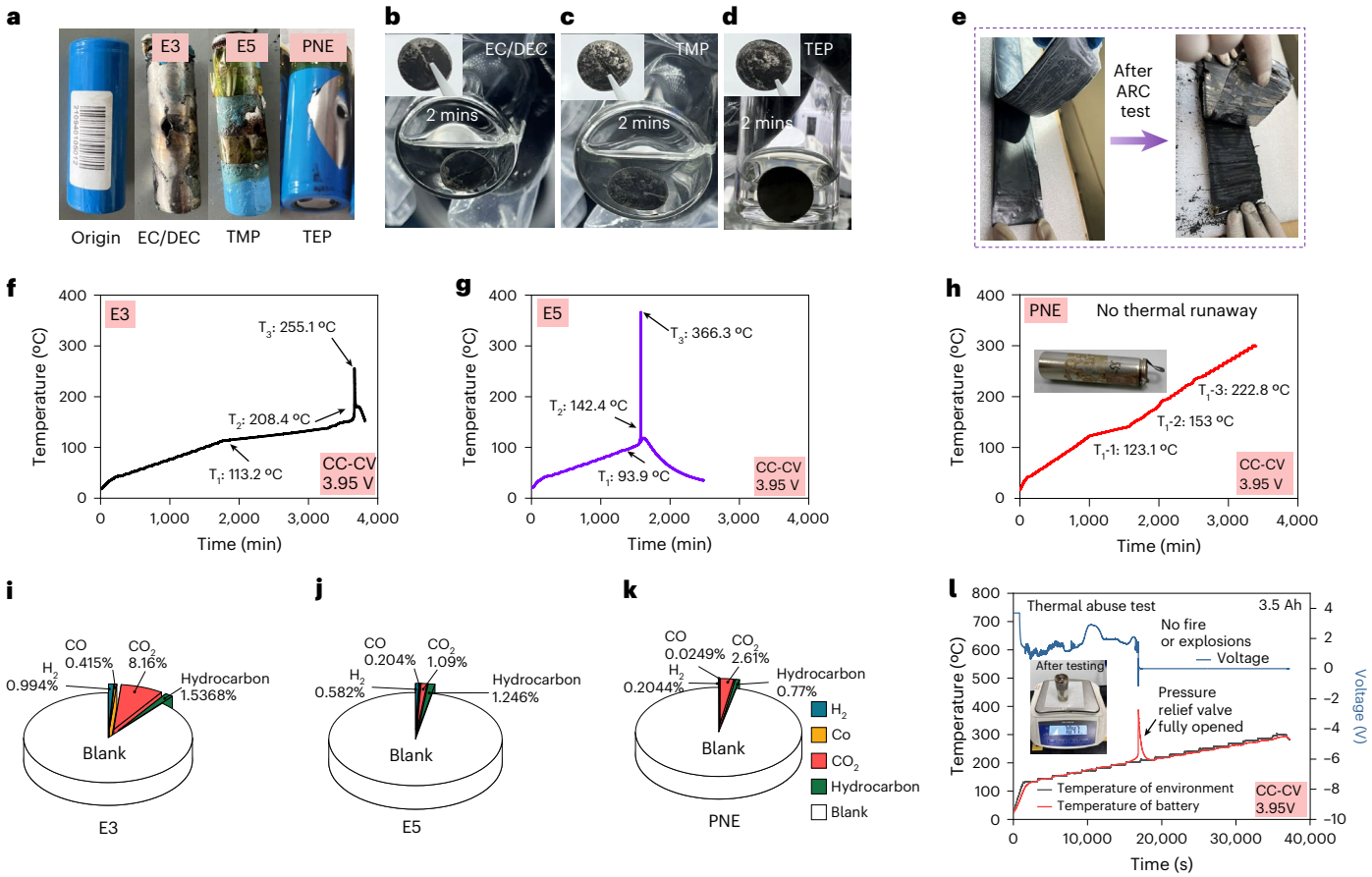

Fig. 4 | The safety test of the cells. a, Nail-penetration tests of E3 (EC/DEC-based), E5 (TMP-based) and PNE (TEP-based). **b**–**d**, Immersion tests of sodium-deposited HC anodes soaked in EC/DEC (**b**), TMP (**c**) and TEP (**d**) solvents. The sodium-deposited HC anode is discharged to 4.0 mAh at 0.2 C (1 C = 300 mAh g^{-1}) current density. The loading mass of HC anode is 6.46 mg cm^{-2}. **e**, Photos of the internal changes of the battery cell before and after the ARC test. After the ARC test, the separator is completely melted and the positive and negative electrode materials are adhered together. **f**–**h**, ARC tests time–temperature curves of E3- (**f**), E5- (**g**) and PNE-based (**h**) 1.45-Ah 18650 cylindrical cells. T_1 was defined as the onset temperature of self-heating, which results from the onset of the chain reactions inside the battery, leading to a spontaneous and continuous rise in temperature if the battery is kept under a poor heat dissipation condition or an almost adiabatic condition. T_2 was defined as the trigger temperature of thermal runaway preset at the dT/dt of 1 °C s^{-1}. T_3 was defined as the maximum temperature during the thermal runaway, which is a key parameter in the evaluation of the destructiveness of thermal runaway. **i**–**k**, Analysis of gas production during ARC tests by gas chromatography of E3 (**i**), E5 (**j**) and PNE (**k**). **l**, Thermal abuse test of 3.5-Ah cylindrical cell. The original weight is 83.91 g. The mass reduction mainly originates from the evaporation of the electrolyte and the escape of gases generated by decomposition reactions.

the nail-penetration process, the maximum temperature of the outer cell case in the TEP system was only increased to 95.2 °C. It is notable that because TMP has a higher content of phosphorus, it should theoretically have better flame-retardant properties compared to TEP. However, its ability to inhibit thermal runaway is inferior to that of TEP. It is reasonable to conclude that the non-flammability of electrolytes does not necessarily guarantee the suppression of thermal runaway, especially in ampere-hour-level batteries. The reason for this inequality is not only related to the higher interfacial stability between the electrodes and PNE, but may also be because that TEP can quickly consume the active sodium precipitated locally during the puncture process, inhibiting the further occurrence of thermal runaway (Fig. 4b–d). In contrast, the reaction of metallic sodium in the TMP solvent is very slow, and the reaction is even slower in EC/DEC. Such non-passivated and active sodium will aggravate the side reactions and facilitate the thermal runaway (Supplementary Fig. 13 and Supplementary Video 9).

To further verify the safety of the designed electrolyte, we conducted a thermal runaway experiment using accelerating rate calorimeter (ARC). In the ARC experiment, T_1 represents the onset temperature for self-heating; T_2 denotes the triggering temperature for thermal runaway and T_3 indicates the maximum temperature during thermal runaway. Therefore, a safer battery is ideally with higher T_1 and T_2, but lower T_3[6]. The ARC tests were conducted using 1.45-Ah 18650 and 3.5-Ah 26700 cylindrical cells. The cells were first preprocessed by charging at a constant current of 0.2 C to 3.95 V, followed by constant voltage charging until the current reached 0.05 C. The detection sensitivity of the instrument was set at 0.02 °C min^{-1} and the temperature increase step was 5 °C. For the pure carbonate-based cell, T_1, T_2 and T_3 were measured at 113.2 °C, 208.4 °C and 255.1 °C, respectively (Fig. 4f). Unexpectedly, the thermal stability of TMP-based cells is even worse with lower T_1 (93.9 °C) and T_2 (142.4 °C) and higher T_3 (366.3 °C) (Fig. 4g). Conversely, the PNE-based cell did not experience thermal runaway even when heated to 300 °C, neither in the 1.45-Ah cell nor in the 3.5-Ah cell (Fig. 4h and Supplementary Fig. 14). Three different onset temperatures (T_1) of 1.45-Ah cell were detected at distinct stages with values of 123.1 °C (T_1-1), 153 °C (T_1-2) and 222.8 °C (T_1-3), respectively. After that, the system did not detect thermal runaway but initiated a stepwise temperature increase even to 300 °C.

The PNE-based cell upon the ARC test was disassembled, and the separator had melted (Fig. 4e), while the electrodes still maintained their integrity (Supplementary Fig. 15). This could be a result of electrolyte polymerization at elevated temperatures, where the polymerized PNE adheres to the surfaces of the cathode and anode materials, binding them together. At the same time, it can prevent direct contact

https://doi.org/10.1038/s41560-026-02032-7

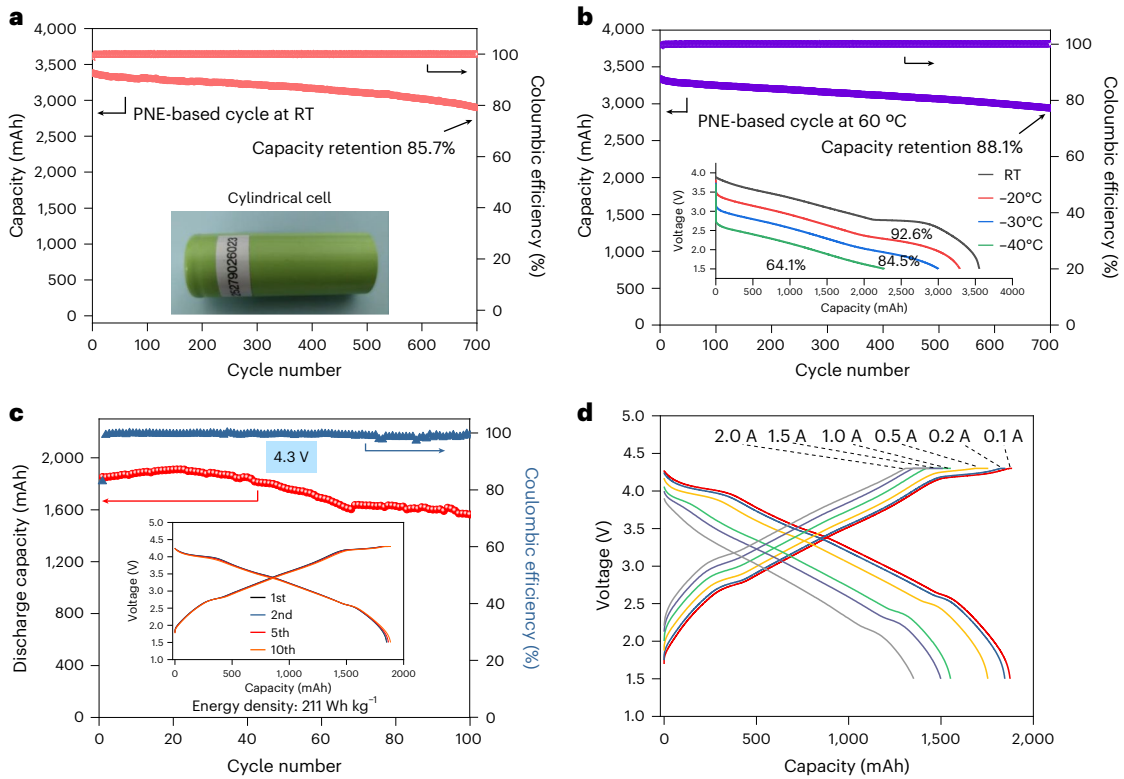

Fig. 5 | Electrochemical performance of cylindrical cells. a,**b**, The cycling performance of O3-$NaCu_{1/9}Ni_{2/9}Fe_{1/3}Mn_{1/3}O_2$ // HC 26700 cylindrical cells with PNE under room temperature (RT) (**a**) and 60 °C (**b**) at a current rate of 0.5 C (1 C = 3.5 A). The embedded diagram in **b** represents the discharge curve resulting from charging at room temperature and discharging at low temperatures at a current of 0.2 C (1 C = 3.5 A). **c**,**d**, The cycling performance of (**c**) and the rate performance of (**d**) 18650 cylindrical cells between 1.5–4.3 V. The embedded diagram in **c** represents the charge–discharge curves.

between the cathode and anode materials, thereby preventing short circuits and crosstalk reactions. Therefore, we speculate that the detected three T_1 peaks may have originated from the exothermic stages caused by the melting of the separator. Subsequently, the polymerization of PNE started at around T_1-2, making the block between anode and cathode, so that the further thermal runaway could be eliminated. A series of Fourier-transform infrared (FTIR) spectroscopy experiments of the PNE heated at different temperatures were conducted to further study its polymerization behaviour. The results verified that the PNE electrolyte began to exhibit significant polymerization behaviour starting at 150 °C (Supplementary Fig. 16), which is close to T_1-2, indicating that polymerization of the electrolyte has already begun around the T_1-2 temperature, which is consistent with the ARC results. This may also be an important reason that TMP-based electrolyte with a higher phosphorus content and excellent non-flammability is far less safe than PNE.

Furthermore, throughout the entire testing period, the heating rate of the PNE system remains considerably lower than those of the E3 (carbonate-based) and E5 (TMP-based) systems (Supplementary Fig. 17). It is crucial that after the ARC test, both E3 and E5 systems generate a significant amount of reducing gases (such as H_2 and CO), whereas the PNE system hardly produced such reducing gas components but only trace amount (0.0244%) of H_2, which is speculated to be originated from the decomposition of trace water during the battery formation process (Fig. 4i–k).

To further verify the safety of the system, we conducted a thermal abuse test using a 3.5-Ah 26700 cylindrical cell to be heated up to 300 °C (Fig. 4l). Although there was a sudden temperature rise occurred at around 200 °C during a 30-minute constant temperature holding period that was due to the released high-temperature steam that contacted the thermocouple with the cell's pressure relief valve fully opened, neither combustion and explosion, nor any sparking was detected throughout the process with the cell's structure remained intact. The thermal abuse test further demonstrated the superior safety of the PNE-based cell. The origin of such safety performance of the PNE-based batteries can be attributed to the synergy between the nature of the thermally induced polymerization of TEP-based electrolyte at high temperature and the optimization of solvation structure and interfacial chemistry by the salts, which can prevent the mechanical/chemical crosstalk between the cathode and the anode and the interface failure and reductive gases generation, inhibiting further thermal runaway in the battery.

Moreover, commercial cells are usually overserved to generate reducing gases during high-temperature storage, which is also a serious safety hazard. Consequently, we performed gas chromatography tests on the gases generated within the E3 and PNE pouch cells after storage at 60 °C. The original gas chromatographic collection is illustrated in Supplementary Fig. 18. Hydrogen production poses a critical risk to battery safety as it can trigger a series of thermal runaway chain reactions, further exacerbating the safety hazards associated with batteries. Unlike conventional carbonate electrolyte systems that typically contain a high proportion H_2 of 19%, the PNE-based system developed in this work showed no detectable generation of hydrogen gas (Supplementary Fig. 19). This observation provides further evidence that the designed battery system with PNE electrolyte is safe. In addition, in the high-temperature storage experiment, the PNE-based cell can present an impressive capacity retention of 94% after 35 days (Supplementary Fig. 20).

Electrochemical performance of the cylindrical cell with PNE electrolyte

On the basis of the battery-level thermal stability with the designed PNE electrolyte, its practical electrochemical performance was further

investigated in the 26700 cylindrical cells. Using CNFM as cathode and HC as anode with the designed PNE electrolyte, the cell possesses a capacity of 3.5 Ah and can endure up to 700 cycles at room temperature with 85.7% capacity retention (Fig. 5a). Moreover, it demonstrates exceptional durability even under high-temperature conditions of 60 °C, allowing for stable cycling up to 700 cycles with 88.1% capacity retention. Besides, excellent discharge capacity retention can be remained at low temperature environments of −20 °C (92.6%), −30 °C (84.5%) and −40 °C (64.1%), respectively (Fig. 5b). The performance comparison of E3, E5 and PNE is shown in Supplementary Fig. 21.

The remarkable achievement can also lie in the successful integration of PNE electrolyte with a high-voltage single crystalline O3-$Na_{0.95}Ni_{0.4}Fe_{0.2}Mn_{0.4}O_2$ (SC-NFM424)[51] cathode cell, resulting in a significantly elevated specific energy density of 211 Wh kg^{-1} within the voltage range of 1.5–4.3 V in an 18650 pouch cylindrical cell with the capacity of 1,874 mAh (Fig. 5c). The detailed design parameters of the cell are provided in the Supplementary Table 4 and Supplementary Fig. 22. The cell demonstrates an excellent cycling stability over 100 cycles at such high energy density. Even at a large current of 2.0 A, it can release a capacity of 1,352 mAh (Fig. 5d). The stringent nail-penetration test was also applied to this 211 Wh kg^{-1} cell at fully charged state at 4.3 V. As shown in Supplementary Video 10, the cell exhibited no smoke, no fire and no explosion, further confirming the superior safety of PNE in such high-voltage and high-energy system.

Conclusions

In this contribution, we have successfully achieved thermal runaway-free ampere-hour-level NIBs by developing a non-flammable electrolyte with thermally induced polymerization (PNE). The electrolyte undergoes polymerization at high temperature with an endothermic process to prevent the thermal side reactions from mechanical/chemical crosstalk between electrodes. The incorporation of both BF_4^- and PF_6^- anions from the salts plays a crucial role in stabilizing the electrode–electrolyte interfaces by forming a B-rich CEI and a PO_2^--rich SEI. As a result, the designed 3.5-Ah-level cylindrical NIBs achieve a excellent cycling stability and wide operating temperature range (−40 °C to 60 °C) without thermal runaway after nail-penetration test and even at a high temperature of 300 °C. This work provides a principle of electrolyte design beyond non-flammability towards battery safety and paves the way for their future applications in energy storage markets.

Methods

Materials preparation

The layered cathode and carbon anode materials are from HiNa Battery Technology Co. Ltd. Composition of the cathode (total mass loading on a single side of electrode: ~16 mg cm^{-2}) slurry was 92 wt% active materials, 4 wt% conductive carbon and 4 wt% binder. The mass loading of only active cathode materials is ~14.7 mg cm^{-2}. The electrode slurries were casted on Al foil followed by a drying process under vacuum. Composition of the anode (total mass loading on a single side of electrode: ~7.0 mg cm^{-2}) slurry was 92 wt% active materials, 4 wt% conductive carbon and 4 wt% binder. The mass loading of only active cathode materials is ~6.44 mg cm^{-2}. Analytical grade solvents were purchased from Shanshan Technology (purity, >99.95%). Sodium salts were purchased from Rolechem (purity, >99.95%). All chemical reagents are used directly without any further purification. The electrolytes were prepared using the stoichiometric ratio of solvent and metal salt in the glovebox, where the moisture and oxygen contents are controlled less than 0.5 ppm.

Electrochemical measurements

All coin cells were assembled in the Ar-filled glovebox using the CR-2032 type coin cell. The amount of electrolyte used for a coin cell is 50 µl. Glass fibre (Whatman GF/A) plus Celgard membrane was utilized as the separator. The 26700-type cylindrical cells and 18650-type cylindrical cells were assembled in a dry room with −50 °C dew point. The charge and discharge tests of full cells were performed on the Land battery test systems (CT3001A or CT2001A) or Neware battery test system (CT-4008). LSV measurements were obtained on a CHI 600E electrochemical workstation (0.1 mV s^{-1}). LSV measurements were obtained from the Na | |stainless steel cells using different electrolytes at a scan rate of 0.1 mV s^{-1} from the −0.1 V to 5.2 V.

Characterizations

All MS data were acquired on an LTQ Orbitrap XL hybrid mass spectrometer (Thermo Fisher Scientific). A DC bias of 2,000 V was applied at the nozzle to generate an electrospray jet. The Orbitrap ion transfer capillary was held at 275°C, and the capillary and tube lens voltages were set at 0 V to avoid unnecessary in-source fragmentation. The resolution was set to 60,000 for all analyses. All data were analysed using the Qual Browser feature of the XcaliburTM program (version 4.1, Thermo Fisher Scientific). The morphologies of the samples were investigated by TEM (FEI Tecnai G2 F20). Cryo-TEM characterizations were carried out using a JEOL JEM-F200 microscope with a cryo transfer holder (Fischione, model 2550) under cryogenic temperatures (100 K) at 200 kV. The electronic conductivity values were obtained from a four-point-probe conductivity metre (MCP-PD51). The surface chemical state was determined by X-ray photoelectron spectroscopy using a PHI 5000 VersaProbe III instrument (Scanning ESCA Microprobe) with Al Kα X-ray source, 15 kV X-ray beam (analysis area: 200 µm × 200 µm) and Ar^+ rate: 3.9 nm min^{-1} for SiO_2 etching (sputtering). All spectra were calibrated with the C 1*s* photoemission peak at 284.8 eV to correct for the charging effect. FTIR was performed by a Bruker VERTEX 80 V spectrophotometer in attenuated total reflection mode (not transmission mode) in a glovebox. TOF-SIMS (semi-quantitative technique) analysis was conducted with a PHI nano TOF II spectrometer with a 30 keV Bi_1^+ acquisition ion beam and a 1 kV Cs^+ sputtering ion beam for electrodes, respectively. During depth profiling, the typical acquisition area was 200 µm × 200 µm and centred within the Ar^+ 500 µm × 500 µm sputtered area. The DSC tests were conducted on a differential scanning calorimeter (Mettler-Toledo, DSC1) in Ar atmosphere at a scanning rate of 5 °C min^{-1} from 30 °C to 400 °C. All DSC tests were performed in Netzsch Au-plated, high-pressure crucibles. After disassembling the electrode, the material was scraped off the current collector and vacuum dried. Each crucible sample was prepared by combining 5 mg ± 0.5 mg of the dried material with an equal mass of the corresponding electrolyte. All TG–DSC–MS tests were performed in Netzsch Au-plated high-pressure crucibles. Unlike the DSC test container, the Au-plated gasket is perforated to allow gases to escape for compositional analysis. The sample preparation is the same as in the DSC tests. The CNFM // HC full cells were charged to 3.95 V. The desodiated-CNFM cathode electrodes and sodiated HC anode electrodes were disassembled from the charged full cells. Because large-molecule organic reagents tend to clog the capillary line of the gas-analysis system, we prepared the TG–DSC–MS samples by scraping undried electrode materials; the powder mass was kept at ~10 mg to guarantee measurement accuracy. ICP: the anode sheet was opened inside the glovebox and dried under vacuum. Then the powders were scraped from the Al foil and dispersed into 6 ml. HNO_3 in a 300-ml beaker. The slurry was stirred for 10 min and sonicated for 15 min with the subsequent addition of 10 ml DI water. The mixture was then left to dissolve for two days. After filtering, the solution was made up to 100 ml, where 10 ml were taken for measurement. Nail-penetration tests: a nail with a diameter of 3 mm was punctured through the battery. The ARC tests were carried out using a commercial ARC system (THT EV + , Thermal Hazard Technology.) with a detection sensitivity of 0.01 °C min^{-1}. For the heat–wait–search stage, the temperature is increased by 5 °C increments. At each increment, the temperature is held constant for 30 minutes. The process continues until the highest temperature of 300 °C is reached. The thermal abuse

test was conducted in a heated explosion-proof chamber. The chamber was heated from room temperature to 130 °C at a rate of 5 °C min^{-1} and then held at 130 °C for 30 minutes. Subsequently, the temperature was increased in steps of 10 °C, with each temperature point being held for 30 minutes, until the final temperature of 300 °C was reached.

MD simulations

All the MD simulations were performed by MD package GROMACS[52] Four models including 200 Na^+, 200 BF_4^- ions, 800 TEP molecules and 200 Na^+, 200 PF_6^- ions, 800 TEP molecules and 200 Na^+, 200 BF_4^- ions, 800 TMP molecules and 200 Na^+, 200 PF_6^- ions, 800 TMP molecules and 240 Na^+, 200 BF_4^-, 40 PF_6^- ions, 960 TEP, 64 vinylene carbonate (VC) molecules were constructed. The force-field parameters of TEP, TMP and VC molecules were generated by LigParGen web server[53], except for their restrained electrostatic potential (RESP) atomic partial charges. These charges were assigned to each atom based on the electrostatic potential (ESP) charges obtained from the Multiwfn program[54]. The force-field parameters for Na^+, BF_4^- and PF_6^- were obtained from Khan et al.[55]. These molecules were initially packed randomly within a cubic box of size 10 × 10 × 10 nm^3 using Packing Optimization for Molecular Dynamics Simulations (PACKMOL)[56]. All the initial configurations were minimized through steepest descent with a convergence criterion of 500 kJ mol^{-1} nm^{-1}. All the systems were equilibrated using Berendsen barostat[57] to keep the pressure of 1 bar with a time constant of 3 ps. The production runs of 40 ns in NPT ensemble under Nóse–Hoover thermostat[58,59] and Parrinello–Rahman barostat[60] were conducted at 298 K, 313 K, 328 K, 343 K, 360 K and 380 K. For the radial distribution function analysis, the last 5 ns simulations at 298 K were utilized. The last 5 ns simulations across all temperatures were dedicated to analysing the desolvation energy of Na ions analysis. The van-der-Waals interactions was computed with a cut-off distance of 1.2 nm. The particle-mesh Ewald (PME)[61] method with a 1.2 nm real space cut-off was applied for the calculation of electrostatic interactions.

Density functional theory simulations

The Gaussian 16 program[62] was employed to calculate the HOMO and LUMO level of $NaBF_4$, $NaPF_6$, TEP, TMP, DEC and EC. In the density functional theory calculations, geometry optimization was carried out using Lee–Yang–Parr correlation functional (B3LYP)[63] at 6-311 + G(d,p) level.

Data availability

The data supporting the findings of this study are available within the article and its Supplementary Information files.

References

1. Xu, K., Ding, M. D., Zhang, S., Allen, J. L. & Jow, T. R. An attempt to formulate nonflammable lithium ion electrolytes with alkyl phosphates and phosphazenes. *J. Electrochem. Soc.* **149**, A622–A626 (2002).
2. Hou, J. et al. Thermal runaway of lithium-ion batteries employing $LiN(SO_2F)_2$-based concentrated electrolytes. *Nat. Commun.* **11**, 5100 (2020).
3. Du, K. et al. A comprehensive study on the electrolyte, anode and cathode for developing commercial type non-flammable sodium-ion battery. *Energy Storage Mater.* **29**, 287–299 (2020).
4. Du, K., Wang, C., Balaya, P., Gajjela, S. R. & Law, M. A fire-retarding electrolyte using triethyl phosphate as a solvent for sodium-ion batteries. *Chem. Commun.* **58**, 533–536 (2022).
5. Suo, L. et al. A new class of solvent-in-salt electrolyte for high-energy rechargeable metallic lithium batteries. *Nat. Commun.* **4**, 1481 (2013).
6. Sun, H. et al. A safe and non-flammable sodium metal battery based on an ionic liquid electrolyte. *Nat. Commun.* **10**, 3302 (2019).
7. Xu, Z. et al. High-voltage and intrinsically safe electrolytes for Li metal batteries. *Nat. Commun.* **15**, 9856 (2024).
8. Zeng, Z. et al. Non-flammable electrolytes with high salt-to-solvent ratios for Li-ion and Li-metal batteries. *Nat. Energy* **3**, 674–681 (2018).
9. Zhu, G.-R. et al. Non-flammable solvent-free liquid polymer electrolyte for lithium metal batteries. *Nat. Commun.* **14**, 4617 (2023).
10. Meng, Y. et al. Designing phosphazene-derivative electrolyte matrices to enable high-voltage lithium metal batteries for extreme working conditions. *Nat. Energy* **8**, 1023–1033 (2023).
11. Ota, H., Kominato, A., Chun, W.-J., Yasukawa, E. & Kasuya, S. Effect of cyclic phosphate additive in non-flammable electrolyte. *J. Power Sources* **119–121**, 393–398 (2003).
12. Zeng, Z. et al. A safer sodium-ion battery based on nonflammable organic phosphate electrolyte. *Adv. Sci.* **3**, 1600066 (2016).
13. Feng, X., Ren, D. & Ouyang, M. Safety of lithium battery materials chemistry. *J. Mater. Chem. A* **11**, 25236–25246 (2023).
14. Wang, Q. et al. Thermal runaway caused fire and explosion of lithium ion battery. *J. Power Sources* **208**, 210–224 (2012).
15. Zheng, Q. et al. A cyclic phosphate-based battery electrolyte for high voltage and safe operation. *Nat. Energy* **5**, 291–298 (2020).
16. Yao, X. L. et al. Comparative study of trimethyl phosphite and trimethyl phosphate as electrolyte additives in lithium ion batteries. *J. Power Sources* **144**, 170–175 (2005).
17. Jiang, X. et al. A nonflammable Na^+-based dual-carbon battery with low-cost, high voltage, and long cycle life. *Adv. Energy Mater.* **8**, 1802176 (2018).
18. Wang, X., Yasukawa, E. & Kasuya, S. Nonflammable trimethyl phosphate solvent containing electrolytes for lithium-ion batteries: I. fundamental Properties. *J. Electrochem. Soc.* **148**, A1058–A1065 (2001).
19. Jia, H. et al. Is nonflammability of electrolyte overrated in the overall safety performance of lithium ion batteries? A sobering revelation from a completely nonflammable electrolyte. *Adv. Energy Mater.* **13**, 2203144 (2023).
20. Chen, H. et al. Designing advanced electrolytes for high-safety and long-lifetime sodium-ion batteries via anion-cation interaction modulation. *J. Am. Chem. Soc.* **146**, 15751–15760 (2024).
21. Liu, X. et al. High capacity and cycle-stable hard carbon anode for nonflammable sodium-ion batteries. *ACS Appl. Mater. Interfaces* **10**, 38141–38150 (2018).
22. Liu, S. et al. An intrinsically non-flammable electrolyte for high performance potassium batteries. *Angew. Chem. Int. Ed.* **59**, 3638–3644 (2019).
23. Shi, P. et al. A highly concentrated phosphate-based electrolyte for high-safety rechargeable lithium batteries. *Chem. Commun.* **54**, 4453–4456 (2018).
24. Xiao, P. et al. A nonflammable electrolyte for ultrahigh-voltage (4.8 V-class) Li||NCM811 cells with a wide temperature range of 100 °C. *Energy Environ. Sci.* **15**, 2435–2444 (2022).
25. Cao, X. et al. Nonflammable electrolytes for lithium ion batteries enabled by ultraconformal passivation interphases. *ACS Energy Lett.* **4**, 2529–2534 (2019).
26. Yang, Z. et al. Fire-retardant, stable-cycling and high-safety sodium ion battery. *Angew. Chem. Int. Ed.* **60**, 27086–27094 (2021).
27. Zheng, X. et al. Bridging the immiscibility of an all-fluoride fire extinguishant with highly-fluorinated electrolytes toward safe sodium metal batteries. *Energy Environ. Sci.* **13**, 1788–1798 (2020).
28. Fan, X. et al. Non-flammable electrolyte enables Li-metal batteries with aggressive cathode chemistries. *Nat. Nanotechnol.* **13**, 715–722 (2018).

29. Wong, D. H. et al. Nonflammable perfluoropolyether-based electrolytes for lithium batteries. *Proc. Natl Acad. Sci. USA* **111**, 3327–3331 (2014).
30. Huang, X.-c. et al. A superior compatible non-flammable electrolyte to hard carbon anodes for robust sodium ion batteries. *New J. Chem.* **48**, 10809–10813 (2024).
31. Xu, K., Zhang, S., Allen, J. L. & Jow, T. R. Nonflammable electrolytes for Li-ion batteries based on a fluorinated phosphate. *J. Electrochem. Soc.* **149**, A1079–A1082 (2002).
32. Zhang, S. et al. Nonflammable electrolyte with low exothermic design for safer lithium-based batteries. *Nano Energy* **114**, 108639 (2023).
33. Wang, Y. et al. Accelerating rate calorimetry studies of the reactions between ionic liquids and charged lithium ion battery electrode materials. *Electrochim. Acta* **52**, 6346–6352 (2007).
34. Huang, Z. et al. A solvent-anchored non-flammable electrolyte. *Matter* **6**, 445–459 (2023).
35. Neupane, S. et al. Shock tube/laser absorption and kinetic modeling study of triethyl phosphate combustion. *J. Phys. Chem. A* **122**, 3829–3836 (2018).
36. Neupane, S., Rahman, R. K., Masunov, A. E. & Vasu, S. S. Theoretical calculation of reaction rates and combustion kinetic modeling study of triethyl phosphate (TEP). *J. Phys. Chem. A* **123**, 4764–4775 (2019).
37. Lhomme, V., Bruneau, C., Soyer, N. & Brault, A. Thermal behavior of some organic phosphates. *Ind. Eng. Chem. Prod. Res. Dev.* **23**, 98–102 (1984).
38. Zhao, Q. et al. Solid-state polymer electrolytes with in-built fast interfacial transport for secondary lithium batteries. *Nat. Energy* **4**, 365–373 (2019).
39. Ma, M. et al. Solvent reorganization and additives synergistically enable high-performance Na-ion batteries. *ACS Energy Lett.* **8**, 477–485 (2022).
40. George, L. et al. Matrix-isolation infrared spectroscopy of organic phosphates. *Appl. Spectrosc.* **48**, 7–12 (1994).
41. Groenewold, G. S. et al. Infrared spectrum of potassium-cationized triethylphosphate generated using tandem mass spectrometry and infrared multiple photon dissociation. *Rapid Commun. Mass Spectrom.* **23**, 2706–2710 (2009).
42. von Wald Cresce, A. et al. Correlating Li^+ solvation sheath structure with interphasial chemistry on graphite. *J. Phys. Chem. C* **116**, 26111–26117 (2012).
43. von Cresce, A. & Xu, K. Preferential solvation of Li^+ directs formation of interphase on graphitic anode. *Electrochem. Solid-State Lett.* **14**, A154–A156 (2011).
44. Xu, K. & von Wald Cresce, A. Li^+-solvation/desolvation dictates interphasial processes on graphitic anode in Li ion cells. *J. Mater. Res.* **27**, 2327–2341 (2012).
45. Sim, R., Su, L., Dolocan, A. & Manthiram, A. Delineating the impact of transition-metal crossover on solid-electrolyte interphase formation with ion mass spectrometry. *Adv. Mater.* **36**, 2311573 (2024).
46. Qi, C. et al. Morphology, structure and thermal stability analysis of cathode and anode material under overcharge. *J. Electrochem. Soc.* **165**, A3985–A3992 (2018).
47. Liu, X. et al. In situ observation of thermal-driven degradation and safety concerns of lithiated graphite anode. *Nat. Commun.* **12**, 4235 (2021).
48. Li, X. et al. Rational design of thermally stable polymorphic layered cathode materials for next generation lithium rechargeable batteries. *Mater. Today* **61**, 91–103 (2022).
49. Liu, X. et al. Thermal runaway of lithium-ion batteries without internal short circuit. *Joule* **2**, 2047–2064 (2018).
50. Seo, D. H. et al. The structural and chemical origin of the oxygen redox activity in layered and cation-disordered Li-excess cathode materials. *Nat. Chem.* **8**, 692–697 (2016).
51. Lian, Z. et al. High-energy Na-ion batteries using single-crystalline cathode. *ACS Energy Lett.* **10**, 1517–1528 (2025).
52. Hess, B., Kutzner, C., van der Spoel, D. & Lindalh, E. GROMACS 4: algorithms for highly efficient, load-balanced, and scalable molecular simulation. *J. Chem. Theory Comput.* **4**, 435–447 (2008).
53. Dodda, L. S., Cabeza de Vaca, I., Tirado-Rives, J. & Jorgensen, W. L. LigParGen web server: an automatic OPLS-AA parameter generator for organic ligands. *Nucleic Acids Res.* **45**, W331–W336 (2017).
54. Lu, T. & Chen, F. Multiwfn: a multifunctional wavefunction analyzer. *J. Comput. Chem.* **33**, 580–592 (2012).
55. Khan, M. S., Karatrantos, A. V., Ohba, T. & Cai, Q. The effect of different organic solvents and anion salts on sodium ion storage in cylindrical carbon nanopores. *Phys. Chem. Chem. Phys.* **21**, 22722–22731 (2019).
56. Martinez, L., Andrade, R., Birgin, E. G. & Martinez, J. M. PACKMOL: a package for building initial configurations for molecular dynamics simulations. *J. Comput. Chem.* **30**, 2157–2164 (2009).
57. Berendsen, H. J. C., Postma, J. P. M., van Gunsteren, W. F., DiNola, A. & Haak, J. R. Molecular dynamics with coupling to an external bath. *J. Chem. Phys.* **81**, 3684–3690 (1984).
58. Nosé, S., A molecular dynamics method for simulations in the canonical ensemble. *Mol. Phys.* **52**, 255–268 (1984).
59. Hoover, W. G. Canonical dynamics: equilibrium phase-space distributions. *Phys. Rev. A Gen. Phys.* **31**, 1695–1697 (1985).
60. Parrinello, M. & Rahman, A. Polymorphic transitions in single crystals: a new molecular dynamics method. *J. Appl. Phys.* **52**, 7182–7190 (1981).
61. Darden, T., York, D. & Pedersen, L. Particle mesh Ewald: an N·log(N) method for Ewald sums in large systems. *J. Chem. Phys.* **98**, 10089–10092 (1993).
62. Frisch, M. E. et al. Gaussian 16 (Gaussian Inc., 2016).
63. Lee, C., Yang, W. & Parr, R. G. Development of the Colle-Salvetti correlation-energy formula into a functional of the electron density. *Phys. Rev. B* **37**, 785–789 (1988).
64. Yu, Y. et al. Non-flammable organic electrolyte for sodium-ion batteries. *Electrochem. Commun.* **110**, 106635 (2020).
65. Jin, Y. et al. Highly reversible sodium ion batteries enabled by stable electrolyte-electrode interphases. *ACS Energy Lett.* **5**, 3212–3220 (2020).
66. Feng, J. et al. Ether-based nonflammable electrolyte for room temperature sodium battery. *J. Power Sources* **284**, 222–226 (2015).
67. Wang, Z. et al. An intrinsically nonflammable electrolyte for prominent safety lithium metal batteries with high energy density and cycling stability. *Adv. Funct. Mater.* **33**, 2215065 (2023).
68. Yang, C. et al. A safe electrolyte enriched with flame-retardant solvents for high-voltage $LiCoO_2$||graphite pouch cells. *ACS Energy Lett.* **9**, 5364–5372 (2024).
69. Xie, Y. et al. Probing thermal and chemical stability of $Na_xNi_{1/3}Fe_{1/3}Mn_{1/3}O_2$ cathode material toward safe sodium-ion batteries. *Chem. Mater.* **30**, 4909–4918 (2018).

Acknowledgements

This work was supported by the National Key R&D Program of China (2022YFB2402500, Y.-S.H.), National Natural Science Foundation (NSFC) of China (52394170-52394174, Y.-S.H.; 22522310, 22339001 H.M.), Commanding Heights of Science and Technology of Chinese Academy of Science (LDES150000, Y.-S.H.), Strategic Priority Research Program of the Chinese Academy of Sciences (XDA0400000, Y.-S.H.), Beijing–Tianjin–Hebei Natural

Science Foundation Cooperation Project (B2024208091, F.X.), the Jiangsu Provincial Carbon Peak and Neutrality Innovation Program (Industry Tackling on Prospect and Key Technology), China (grant number BE2022002-5, Y. Lu), International Partnership Program of Chinese Academy of Sciences (005GJHZ2023021MI, Y.-S.H.) and the 10th Young Elite Scientists Sponsorship Program by CAST (F.X.). We are especially grateful to B. Wang for his invaluable assistance with the TG–DSC–MS testing during the revision of this manuscript.

Author contributions

Y.-S.H. conceived and designed the research. J.Z. performed the experiments with L.Z. J.Z. assembled the cylindrical cells and soft pouch cells. H.W. provided positive electrode material. H.M. carried out the simulation work. S.W and Xuefeng Wang completed the cyro-TEM experiments. S.H. completed the IR experiments. Z.C. and Xubin Wang completed the X-ray photoelectron spectroscopy experiments. F.D. participated in the analysis of test results. Y. Liu and Y.Y. conducted the gas production analysis. L.C. conceived and designed the experiments. J.Z., F.X., Y. Lu and Y.-S.H. wrote the manuscript. All authors participated in analysing the experimental results and preparing the manuscript.

Competing interests

The authors declare no competing interests.

Additional information

Supplementary information The online version contains supplementary material available at https://doi.org/10.1038/s41560-026-02032-7.

Correspondence and requests for materials should be addressed to Fei Xie, Huican Mao, Yaxiang Lu or Yong-Sheng Hu.

Peer review information *Nature Energy* thanks Gui-Liang Xu and the other, anonymous, reviewer(s) for their contribution to the peer review of this work.